ACS Catalysis

pubs.acs.org/acscatalysis

Research Article

Role of OH Intermediates during the Au Oxide Electro-Reduction at Low pH Elucidated by Electrochemical Surface-Enhanced Raman Spectroscopy and Implicit Solvent Density Functional Theory

Jonas H. K. Pfisterer, Francesco Nattino, Ulmas E. Zhumaev, Manuel Breiner, Juan M. Feliu, Nicola Marzari, and Katrin F. Domke*

Cite This: *ACS Catal.* 2020, 10, 12716–12726

Read Online

ACCESS | Metrics & More | Article Recommendations | Supporting Information

ABSTRACT: Molecular understanding of the electrochemical oxidation of metals and the electro-reduction of metal oxides is of pivotal importance for the rational design of catalyst-based devices where metal(oxide) electrodes play a crucial role. *Operando* monitoring and reliable identification of reacting species, however, are challenging tasks because they require surface-molecular sensitive and specific experiments under reaction conditions and sophisticated theoretical calculations. The lack of molecular insight under operating conditions is largely due to the limited availability of *operando* tools and to date still hinders a quick technological advancement of electrocatalytic devices. Here, we present a combination of advanced density functional theory (DFT) calculations considering implicit solvent contributions and time-resolved electrochemical surface-enhanced Raman spectroscopy (EC-SERS) to identify short-lived reaction intermediates during the showcase electro-reduction of Au oxide (AuOx) in sulfuric acid over several tens of seconds. The EC-SER spectra provide evidence for temporary Au-OH formation and for the asynchronous adsorption of (bi)sulfate ions at the surface during the reduction process. Spectral intensity fluctuations indicate an OH/(bi)sulfate turnover period of 4 s. As such, the presented EC-SERS potential jump approach combined with implicit solvent DFT simulations allows us to propose a reaction mechanism and prove that short-lived Au-OH intermediates also play an active role during the AuOx electro-reduction in acidic media, implying their potential relevance also for other electrocatalytic systems operating at low pH, like metal corrosion, the oxidation of CO, HCOOH, and other small organic molecules, and the oxygen evolution reaction.

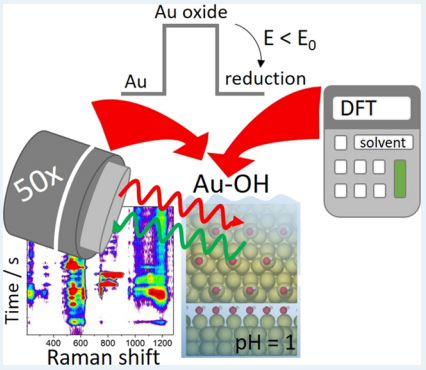

KEYWORDS: *gold oxide, implicit solvent, operando SERS, potential jump, electrochemical reduction*

1. INTRODUCTION

The rational design of efficient electrocatalysts and of effective measures against metal corrosion requires detailed molecular understanding of the underlying reaction mechanisms and thus of the surface chemistry under realistic working conditions.[1−3] Elucidating catalytic reaction pathways by monitoring and identifying reaction intermediates, such as adsorbed OH species, can provide the necessary insight to strategically modify the electrode surface structure and/or material composition to engineer surface reactivity, selectivity, and stability.[4] However, detection and reliable identification of surface reaction intermediates under reaction conditions are demanding[5] and require sophisticated experimental and theoretical tools. Due to the typically low residence times (μs to s[6,7]) of the molecular adsorbates at the surface and a limited number of available active surface sites,[8] experimental techniques with high sensitivity are required. The need for measurements under realistic working conditions additionally poses technical challenges due to the liquid environment and the necessary potential control. For example, the detection of reacting OH species during electrocatalytic oxygen reduction or noble metal corrosion reactions constitutes a huge challenge on the route to clarifying proposed reaction mechanisms.[9−11] The combined efforts of advanced theoretical calculations and highly sensitive spectro-electrochemical tools that provide surface-molecular sensitivity and chemical specificity under realistic working conditions are therefore required.

One of the most widely spread electrochemical (model) systems of fundamental interest, for example, as an electrocatalyst, catalyst support, or corrosive material, is the Au electrode. Often during electrocatalytic reactions, an Au oxide (AuOx) film is formed on the Au surface, which decisively alters the Au electrode's properties. However, despite long-

Received: June 23, 2020
Revised: September 26, 2020
Published: October 19, 2020

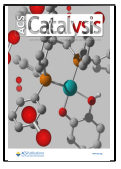

standing research efforts, the formation mechanism(s), the exact nature of the electrochemically generated AuOx, and its electro-reduction pathways are still not fully understood. Understanding the mechanism of formation and reduction of surface AuOx is of particular importance to improve, for example, protocols for anodic catalytic oxidation of small organic molecules and to enhance water splitting efficiency at anodic potentials where, at least partly, the required oxygen atoms are provided by the oxide surface.[12] Under OER conditions, partly hydrated AuOx[13] and likely incorporated OH species[14] compose the catalytically active sites, as pure AuOx is thermodynamically unstable. In the reverse ORR reaction, Au-OH species have been postulated to promote high ORR activity.[15] Furthermore, Au-OH species are of particular importance for the electrocatalytic oxidation of CO and HCOOH, where $CO/HCOO^-$ and adsorbed OH can react to form CO_2.[16,17] Hydroxyl groups available at an (Au) catalyst surface are known to substantially influence reaction rates and are as such of crucial interest for the CO and alcohol oxidation both in liquid and in gas phase catalysis.[18]

Based on the observation of an unusually broad and asymmetric vibrational band around 580 cm^{-1}, Weaver and co-workers hypothesized that the AuOx surface − the starting point for electro-reduction as well as water splitting − is composed of a "wide multiplicity of surface oxide structures formed simultaneously, possibly involving different coordination geometries and hydration states of the Au atoms".[19] However, clear-cut experimental evidence to identify different (hydr)oxide species during Au electro-reduction/oxidation in acidic media has remained elusive due to the scarce availability of *operando* spectroscopic techniques and the chemical complexity of the broad AuOx feature. In neutral and alkaline media, electrochemical shell-isolated nanoparticle-enhanced Raman spectroscopy (EC-SHINERS) revealed an OH-bending mode at 790 and 807 cm^{-1}, respectively, indicating the involvement of OH species in the oxidation/reduction mechanism.[10,20] In acidic media, it is typically assumed that AuOx reduction and Au oxidation also proceed via the formation of Au-OH intermediates.[21] For example, Au-OH species have been proposed as key intermediates during oxide film formation[12,22] or during the oxygen evolution reaction (OER)[23] at low pH. However, Au-OH species at low pH have, to the best of our knowledge, not yet been observed experimentally to date, and as such a validation of the proposed oxidation/reduction mechanism is still missing.

Experimentally, electrochemical surface-enhanced infrared absorption spectroscopy (EC-SEIRAS) has provided molecular insight into potential-dependent ion adsorption on Au electrodes[24] but is limited to higher wavenumber regions (typically >1000 cm^{-1}). The low wavenumber region between 0 and 1000 cm^{-1}, however, carries relevant information on molecule-metal surface interactions. Raman spectroscopy covers lower wavenumber regions and is less hindered by absorption of water in comparison to IR spectroscopy. The usually rather low Raman scattering cross-sections can be elegantly bypassed by EC-SERS, where nanoscale-rough metal surfaces enhance the otherwise weak Raman signals and provide the required high surface-molecular sensitivity and chemical specificity,[25] sufficient even for time-resolved measurements in the sub-second regime.[26] In terms of theory, recent progress in density functional theory (DFT) simulations considering implicit solvent models allows advanced calculations of molecular vibrations at solid−liquid interfaces, potential-dependent stability investigations, and a reliable interpretation of experimentally gathered spectroscopic data.[27]

Here, we aim to identify the short-lived reaction intermediates during the electro-reduction of AuOx with a combined experimental and simulation approach. Advanced DFT calculations that consider electrolyte contributions on an implicit level together with a powerful experimental approach based on potential-jump EC-SERS experiments allow us to elucidate the evolution of reactive surface species, such as OH, Au oxide, and sulfate species, over several tens of seconds in increments of 0.5 s under reaction conditions in acidic media. The EC-SER spectral fingerprint gives evidence for temporary Au-OH formation, for the existence of an Au oxide phase resembling the bulk Au_2O_3 coordination, and for the presence of sulfate ions at the surface. Spectral intensity oscillations of OH and sulfate bands with a period of about 4 s suggest that the mechanistic steps are strongly coupled. Our results allow us to propose a mechanism for oxidation/reduction reactions where adsorbed OH species are likely to play an important role at low pH, for example, in the OER and oxygen reduction reaction (ORR) and in corrosion phenomena.

2. METHODS

2.1. Experimental Section. The polycrystalline Au electrode (EDAQ ET053-1 Au disc electrode, 3 mm Au disc in 6 mm OD PEEK body) was electrochemically roughened following the procedure by Tian and co-workers.[28] The roughening was performed in 0.1 M KCl (99.999%, Suprapur, Merck) solution with an Au wire as a counter electrode (0.5 mm diameter, Alfa Aesar, Premion, 99.9985% metals basis) and a commercial Ag/AgCl reference electrode (3 M KCl, SI Analytics). The Au electrode was kept at −0.3 V vs Ag/AgCl for 30 s, then ramped to 1.2 V vs Ag/AgCl with a scan rate of 1 V/s, and held at this potential for 1.2 s. Afterward, the potential was ramped back to −0.3 V vs Ag/AgCl with an adjusted scan rate of 0.5 V/s and again held at −0.3 V vs Ag/AgCl for 30 s. This procedure/cycle was repeated 25 times leading to a brownish/red color of the Au electrode. Subsequently, the Au electrode was thoroughly rinsed with and stored in MilliQ water (Millipore-Q, 18 MΩ cm) to remove any possible contaminants adsorbed during the roughening procedure. The Au electrode was additionally cleaned by immersion in 0.1 M H_2SO_4 for 1 h before sample mounting.

The EC-SERS setup is home built and based on an Olympus 50x long working-distance objective (NA = 0.5, working distance = 10.6 mm), a red HeNe laser (632.8 nm, linearly polarized, max. output power = 35 mW), and a Horiba iHR 550 spectrograph with a nitrogen-cooled CCD detector (Symphony II, Horiba) controlled by LabSpec 5 software. A backscattering configuration with an edge filter and a 600 lines/mm grating was employed for the reported experiments. An additional CMOS camera (MC 1362, Mikrotron) temporarily coupled into the beam path with a beam splitter allowed proper focusing of the laser beam onto the Au surface. The laser power of ∼20 mW at the laser focus spot was measured in air and is comparable to the laser power reported in other EC-SERS studies.[19] Due to optical aberrations at the glass window, the power was estimated to be reduced to around 5 to 7 mW at the sample. Acquisition times between 0.5 and 1 s were used. To compensate for changes in the overall SERS background, we analyze background-subtracted data (see the Supporting Information for details). A

https://dx.doi.org/10.1021/acscatal.0c02752
ACS Catal. 2020, 10, 12716−12726

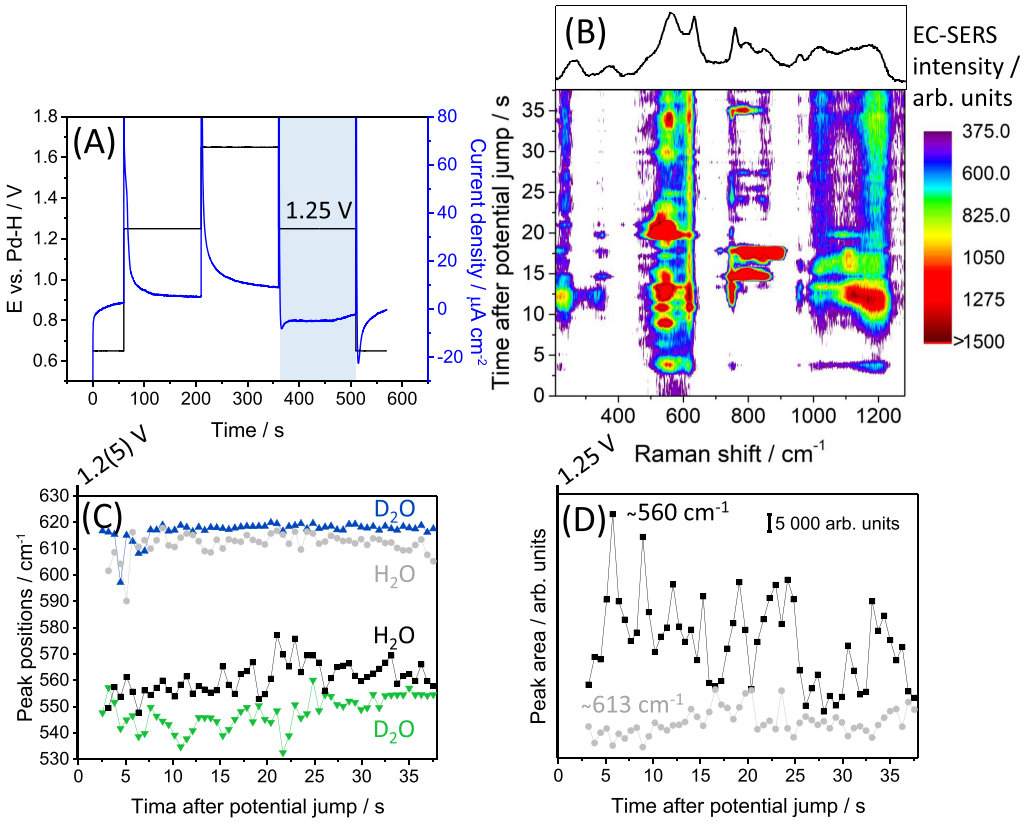

Figure 1. EC-SERS potential jump experiments. (A) Applied electrode potentials as a function of time for the potential jump sequence (black line) and the corresponding current vs time traces (blue line) in 0.1 M H_2SO_4 (D_2O-based electrolyte). (B) EC-SERS intensity map as a function of time for the first 38 s after the potential-jump from 1.65 V to 1.25 V vs Pd-H, recorded at 0.5 s spectral acquisition time. Top: Averaged EC-SER raw spectrum (black line). (C) Comparison of peak positions of the double peak feature in the 530 to 630 cm^{-1} spectral region in H_2O- and in D_2O-based experiments. (D) Peak areas of the ~560 and ~613 cm^{-1} Raman bands as a function of time after the potential jump from 1.6 to 1.2 V vs Pd-H in H_2O-based electrolyte.

Schlumberger (SI 1286 Electrochemical Interface) potentiostat controlled by CorrWare software was used for the EC-SERS measurements. An Au wire (0.5 mm diameter, Alfa Aesar, Premion, 99.9985% metals basis) and a freshly prepared hydrogen-loaded Pd wire (Pd-H; 0.5 mm diameter, MaTecK, 99.95% metals basis) were used as counter and reference electrodes, respectively. The Pd-H reference electrode was prepared by applying 10 V between the Pd wire and an Au counter electrode in 0.1 M H_2SO_4 until the evolution of hydrogen gas roughly corresponded to the oxygen gas bubble formation. The Pd-H reference electrode was freshly prepared before each experiment and, for a pH of 1 (as used in this study), corresponds to the reversible hydrogen electrode at pH ≈ 0 (i.e., SHE). The aqueous electrolytes were 0.1 M H_2SO_4 (96%, Suprapur, Merck) prepared from either MilliQ water (Millipore-Q, 18 MΩ cm, Merck) or deuterated water (deuterium oxide, 99.9 atom % D, Sigma-Aldrich). The electrolytes were degased with Ar (Westfalen, 6.0 N) before transfer to the Teflon cell. The Teflon cell and all glassware were boiled in ~40% HNO_3 (≥65%, Sigma-Aldrich). The glass cell window (thickness: 1 or 2 mm, diameter: 25.4 mm, PLANO GmbH) and Kalrez-F sealing ring (6 mm x 2 mm, VOXTEC) were cleaned in Piranha solution (H_2SO_4 (96%)/ H_2O_2 (30%) ratio of 3:1). After chemical cleaning, all items were boiled in MilliQ water three times with thorough rinsing using fresh MilliQ between each boiling step.

Additional CV measurements were performed with a Metrohm Autolab PGSTAT 30 multipotentiostat using NOVA 2.1.2 software. The working electrode was a polycrystalline Au electrode used for the EC-SERS experiments but without the additional roughening procedure. An Au wire and a Pd-H wire were used as counter and reference electrodes, respectively. The Pd-H reference electrode was prepared according to the procedure specified above. Argon gas (Westfalen, 6.0 N) was used to degas the 0.1 M H_2SO_4 electrolyte (Milli-Q based) for 30 min and to blanket the solution. To electrochemically clean the working electrode, five CV scans between 0.55 and 1.6 V vs Pd-H were performed before each measurement at a 100 mV/s scan rate.

2.2. Computational. DFT calculations were performed with the Quantum-ESPRESSO (QE) distribution,[29,30] using the Perdew−Burke−Ernzerhof exchange-correlation functional[31] and pseudopotentials[32−34] from the Standard Solid State Pseudopotentials library[35] (SSSP v1.0 efficiency). Plane-waves up to a kinetic energy of 45 Ry (360 Ry) were included in the basis set for the expansion of the wavefunction (electron density). The Au surface was modeled by means of a 5-layer Au(111) slab constructed from the relaxed bulk lattice constant a = 4.151 Å. The two uppermost layers were allowed to relax, while the remaining atomic layers were kept frozen in the bulk configuration. Periodic replicas of the slab were separated by 15 Å of vacuum, and a real-space dipole correction was applied along the surface normal.[36] We considered a (2×2) supercell of the primitive surface unit cell, using a Γ-centered (11×11×1) k-point mesh to sample the first Brillouin zone. A Marzari-Vanderbilt smearing[37] with a

https://dx.doi.org/10.1021/acscatal.0c02752
ACS Catal. 2020, 10, 12716−12726

width parameter of 0.02 Ry was employed. Spin-polarized calculations were performed for the interfaces that presented a nonzero magnetic moment.

To account for the presence of the electrochemical environment, we made use of continuum solvation as implemented in the ENVIRON module[38] for QE. The slabs were embedded in a polarizable dielectric medium with a water dielectric constant of ε_0 = 78.3. A smooth cavity defined as a function of the valence electron density was employed to define the boundary between the quantum-mechanical region and the solvent region. In particular, we used the cavity definition from the revised self-consistent continuum solvation model,[39,40] using the parameterization optimized for neutral isolated systems (ϱ_{max} = 0.005 a.u., ϱ_{min} = 0.0001 a.u., $\alpha + \gamma$ = 11.5 dyn/cm, and β = 0 GPa). The local cavity was augmented with a nonlocal component aiming at avoiding the formation of nonphysical dielectric pockets within regions of the system that are too small to fit a solvent molecule.[41]

Γ-point vibrational frequencies were computed from a finite-difference approach as implemented in the atomic simulation environment package.[42] For a given relaxed structure, the force-constant matrix was constructed from the forces computed for a pool of displaced configurations. In particular, we considered two opposite 0.01 Å displacements per Cartesian direction and atom, including all interface atoms and the Au atoms in the uppermost layer of the slab.

The surface electrochemical stability was investigated using the computational hydrogen electrode (CHE) approach.[43] Under the assumption that only proton-coupled electron transfers occur and that the effect of the potential bias consists in a mere shift of the electron chemical potential, one can estimate the formation energy of a given interface structure using exclusively energies computed for neutrally charged interfaces. The validity of the assumption underlying the CHE was corroborated by additional test calculations performed with a grand-canonical approach[27] where potential and pH effects were decoupled by treating the proton and the electron chemical potentials as free variables (see Figures S1−S3 and Supporting Information for further details).

3. RESULTS

3.1. Experimental Results. We performed EC-SERS potential-jump experiments in which we employed the potential-jump sequence shown in Figure 1A (black curve; D_2O-based electrolyte; see Figure S4 for H_2O-based electrolyte). The potential sequence starts and ends at a potential of 0.65 V vs Pd-H with a pristine Au surface with low sulfate adsorption of less than 4% surface coverage[44,45] followed by an upward potential jump to 1.25 V vs Pd-H that mirrors the downward potential jump to the resting potential after surface oxidation at 1.65 V vs Pd-H. Note that experiments in H_2O-based solutions were performed with a −50 mV potential difference according to the observed shift of the reference electrode potential during CV (Figure S5); i.e., the oxidation potential was 1.6 V vs Pd-H and the resting reduction potential typically 1.2 V vs Pd-H. Figure 1A also shows the recorded current versus time traces for the applied potential steps (blue curve). We find a current plateau when jumping from 1.6(5) to 1.2(5) V vs Pd-H that differs from the exponential current decays observed for the applied potential jumps to other resting potentials (Figure 1A; Figures S6−S8). The current plateau can be slightly tuned in duration by potential variations in the order of ±0.05 V around the reduction onset. For potential jumps to more positive potentials than 1.25 V vs Pd-H, the detected reduction currents are negligible and the AuOx SERS peak remains stable over the course of tens of seconds; i.e., the oxide reduction is significantly slowed down (Figures S6−S8). For potential jumps to more negative potentials than 1.15 V vs Pd-H, the reduction currents show a fast exponential decay (Figures S6−S8) and SERS peaks of reaction intermediates are hardly detectable with our spectral acquisition time of 0.5 s; i.e., the AuOx reduction is too fast to be followed in detail by EC-SERS.

Similar plateau-shaped $I(t)$ traces have been observed earlier during AuOx reduction experiments by Arvia and co-workers.[46] Following the approach suggested by the Arvia group, we tried to fit the plateau-shaped $I(t)$ traces with two functions, one assigned to an instantaneous and the other one assigned to a progressive nucleation and growth model: $I(t) = P_1 \cdot [1 - \exp(-P_2 \cdot t^2)] \cdot \exp(-P_2 \cdot t^2)$ or $I(t) = P_1 \cdot [1 - \exp(-P_3 \cdot t^3)] \cdot \exp(-P_3 \cdot t^2)$. Here, t denotes time; P_1 incorporates the growth-rate constant perpendicular to the surface, while P_2 and P_3 are composed of the growth-rate constant parallel to the surface, the number of nucleation sites, and the density and molecular weight of the formed oxide phase. However, satisfactory fits were not achieved despite the similarity of the investigated system. A second fitting attempt with a related 2D progressive nucleation and growth model suggested by García and Koper,[47] adjusted with variable exponential parameters for different experimental conditions (resting time and potential), $I(t) = R_1 \cdot t^{R_2} \cdot \exp(-R_3 \cdot t^{R_4}) + R_5 \cdot \exp(-R_6 \cdot t)$, gave acceptable results (see Figure S9 for details). Although García and Koper investigated the CO oxidation on Pt electrodes, they observed similarly shaped $I(t)$ traces. In their formalism, the parameters R_1, R_3, R_5, and R_6 include the surface atom, terrace and step site densities, different oxidation rates at those sites, and an OH formation rate. The interested reader is referred to the work by García and Koper[47] for a detailed discussion of the model parameters. Note that, for our data, only introduction of R_2 and R_4 as variable parameters in the exponents provided acceptable fitting results.

Figure 1B shows an EC-SERS intensity map as a function of time after a potential jump to the reduction onset (1.25 V vs Pd-H resting potential, see Figures S10 and S11 and the Supporting Information for further details) and the corresponding averaged EC-SER spectrum (black curve). We observe spectral features with peaks appearing at around 230, 350, 540−620, 750−850, 955, and 1030−1200 cm^{-1}. The relative intensities of the different spectral regions undergo dynamical changes on the second-timescale during the electroreduction of AuOx. Peak positions were determined with Lorentzian peak fitting after linear background subtraction (see the Supporting Information for details). The results of the peak fitting are summarized in Table 1 for experiments in H_2O- and in D_2O-based sulfuric acid electrolytes. The broad peak around 594 cm^{-1} (Table S1) splits into two peaks after a short delay of approx. 1 to 3 s (540−620 cm^{-1} wavenumber region, Figure 1C). The upper peak is located at higher wavenumbers in D_2O at 617.3 ± 0.7 cm^{-1} compared to 612.6 ± 0.2 cm^{-1} in H_2O. The lower peak at 560.4 ± 1.8 cm^{-1} in H_2O is located at 545.5 ± 2.9 cm^{-1} in D_2O. The lower wavenumber peak at ca. 560 cm^{-1} shows oscillations in intensity that last between 50 and 100 s with an average oscillation period of 4.2 ± 1.5 s for both H_2O- and D_2O-based electrolytes (Figures 1B,D and 3). The full width at half maximum (FWHM) of the 560 and 613 cm^{-1} peaks is ∼70 and ∼28 cm^{-1}, respectively, while the 594 cm^{-1}

https://dx.doi.org/10.1021/acscatal.0c02752
ACS Catal. 2020, 10, 12716−12726

Table 1. Peak Positions in H_2O and in D_2O Electrolytes[a]

peak position in H_2O (cm^{-1})	peak position in D_2O (cm^{-1})	Δ peak position	peak assignment
232.7 ± 1.9	233.9 ± 0.9	—	SO_4^{2-} [ref.[48,49]]
350.5 ± 0.6	347.7 ± 1.2	↓	Au--OH (weakly bound) [exp./DFT]
560.4 ± 1.8	545.5 ± 2.9	↓	Au-OH stretching [exp./DFT]
612.6 ± 0.2	617.3 ± 0.7	↑	O-Au(-OH) [exp./DFT]
751.7 ± 4.9	749.7 ± 1.6	—	O-Au-O [exp./ref.[50]]
771.4 ± 3.7	783.7 ± 11.2	—	O-Au-O [exp./ref.[50]]
853.0 ± 1.9	850.7 ± 2.0	—	SO_4^{2-} [DFT/ref.[51]]
956.6 ± 1.0	954.7 ± 0.6	↓	HSO_4^- [exp./ref.[52,53]]
1030.6 ± 5.9	1030.0 ± 4.2	—	SO_4^{2-} [ref.[48,49,54]]
1136.8 ± 21.7	1135.1 ± 29.7	—	SO_4^{2-} [ref.[49,54]]
1190.9 ± 3.8	1197.9 ± 7.2	—	SO_4^{2-} [ref.[24,44,48,49]]

[a]Fitted peak positions in H_2O- and in D_2O-based electrolyte solutions after jumping from 1.6(S) to 1.2(S) V vs Pd-H (see the Supporting Information for details) and peak assignment according to isotope comparison, DFT calculations, and the literature. Black arrows: peak up- or down-shift in D_2O compared to H_2O. (—): within standard deviation.

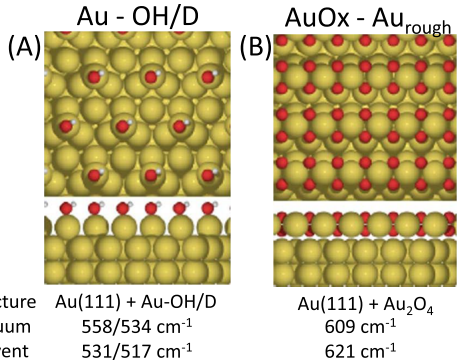

Figure 2. Illustration of two of the most stable interface structures for the calculations of Au-OH and AuOx and their vibrational frequencies in a vacuum and the implicit solvent. Oxygen, hydrogen, and Au atoms are shown in red, gray, and yellow, respectively. For each structure, top and side views are presented. (A) Most stable OH/D-adsorption configuration on the roughened Au surface (adatoms on Au(111)) according to geometry optimization. (B) Illustration of an oxidized structure originating from a 'roughened' surface including two Au adatoms (per unit cell) with four oxygen atoms.

peak showing at 1.6 V vs Pd-H has a FWHM of ∼130 cm^{-1}. The bands at 350.5 ± 0.6 and 956.6 ± 1.0 cm^{-1} in H_2O exhibit a slight difference in the peak position of about 1 to 3 cm^{-1} when comparing to D_2O-based electrolyte experiments (347.7 ± 1.2; 954.7 ± 0.6 cm^{-1}). All other peak positions are independent of isotope exchange (Table 1) according to overlapping standard deviations determined from different experimental rounds.

3.2. Computational Results. Au surfaces were generated starting from the thermodynamically most stable Au termination, i.e., Au(111). We have considered two 'roughened' surfaces in addition to the pristine Au(111) to mimic the rough polycrystalline Au electrode used in the experiments. Specifically, we have modeled surfaces including isolated Au atoms and rows of Au atoms (2 adatoms in the p(2×2) substrate unit cell employed) adsorbed on the Au(111) facet. These surfaces are chosen over kinked and

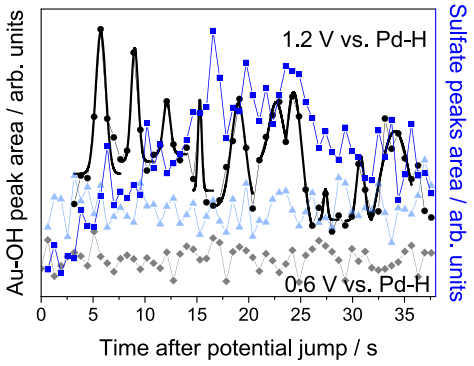

Figure 3. Au-OH and (bi)sulfate EC-SERS intensity oscillations. EC-SERS intensity oscillations of the Au-OH peak at 560 cm^{-1} (black circles) and of the (bi)sulfate peaks (blue squares) at an applied potential of 1.2 V vs Pd-H. Light blue triangles and gray diamonds indicate the background level recorded at 0.6 V vs Pd-H. The solid black lines indicate the Gaussian peak fits to determine the Au-OH oscillation period.

stepped vicinal surfaces since the low coordination number (i.e., higher expected reactivity) of isolated adatoms and adatom rows and their higher accessibility to oxygen atoms make these structures more suited to form Au/O mixed layer structures that result from the electrochemical oxidation/reduction cycles. Vibrational frequencies were computed considering vacuum conditions as well as an implicit solvent model to account for the influence of the aqueous electrolyte. When accounting for the presence of the electrochemical environment through implicit solvents, the computed frequencies of the less polar oxide structures differ only slightly from the ones in a vacuum by about 1 to 4 cm^{-1} (Table S2). Only structures K and L (Table S2) differ by 7 and 12 cm^{-1}, respectively, indicating that for Au_2O_3 and Au_2O_4 screening effects play a more important role than for less coordinated AuOx structures. The OH-based structures shift between 7 and 27 cm^{-1} when taking solvent effects into account due to the strong OH dipole screening by the dielectric medium.

All possible adsorption sites and high-symmetry configurations have been sampled for OH adsorption on the three surfaces. The lowest-energy structures have been considered here, after verifying that they correspond to real minima (no imaginary frequency present). Figure S12A–C illustrates the most stable OH-adsorption configurations on the flat and roughened Au surfaces, while Table S2 (upper panel) reports the computed surface-OH and surface-OD stretch frequencies. For vacuum, the frequencies corresponding to OH/D adsorbed on an Au adatom (Figure 2A) are 558 and 534 cm^{-1}, respectively. When accounting for the solvent effects, the band frequencies are located at lower wavenumbers, also showing a change in the Au-OH/Au-OD wavenumber ratio (531/517 cm^{-1}). Bridging OH species adsorbed on plain Au(111) or on the 'roughened' Au surface show calculated frequencies between 316 and 371 cm^{-1} (see Table S2) and exhibit down-shifts in peak positions of 3 to 6 cm^{-1} upon isotope exchange.

Partially oxidized interfaces were generated by considering oxygen adsorption with a coverage ranging from 0.25 monolayers (ML) to 1 ML on the three different Au surfaces. For each surface stoichiometry, we have explored various initial configurations, testing oxygen adsorption in (combinations of)

https://dx.doi.org/10.1021/acscatal.0c02752
ACS Catal. 2020, 10, 12716−12726

high-symmetry adsorption sites and structures built from physical intuition. Structures that lead to stable interfaces after geometry optimization (i.e., Cartesian components of all forces smaller than 0.0002 atomic units (Ry/Bohr) with no imaginary frequency) are illustrated in Figure S12D−L. The maximum frequencies calculated for these structures are shown in Table S2 (lower panel). We find that the Au-O structures that involve minor surface reconstructions (Figure S12D−F,I) are characterized by a maximum frequency that does not exceed 500 cm^{-1}. Larger frequencies (>550 cm^{-1}) are observed for the interfaces where one or multiple Au atoms are clearly oxygen-coordinated. The largest frequency computed (vacuum: 609 cm^{-1}; solvent: 621 cm^{-1}), corresponding to the structure illustrated in Figure 2B, is characterized by an Au atom in a 4-fold coordination with oxygen, as also observed in the form of bulk Au oxide Au_2O_3.[55] The frequency computed in the implicit solvent for a (partially) protonated structure (i.e., adding an H atom to the structure shown in Figure 2B, see Figure S13) is 601 cm^{-1}, and its frequency is located at 602 cm^{-1} when H is replaced with D.

We have also investigated the relative electrochemical stability of the various interface structures (Figures S1−S3) based on the CHE, which was further verified by a grand-canonical approach (see the Supporting Information for details). Calculations show the clean Au(111) surface to be the most stable interface up to a potential of ∼1.18 V vs Pd-H. Oxygen atom adsorption is predicted to take place at potentials between 1.18 and 1.22 V vs Pd-H, and for >1.22 V vs Pd-H, the interface structure illustrated in Figure 2B becomes the most stable according to CHE calculations.

4. DISCUSSION

4.1. EC-SERS Potential-Jump Approach. EC-SER spectra reveal dynamically evolving spectral features (Figure 1B and S10, S11) when the applied resting potential is around the reduction onset at ∼1.2 V vs Pd-H and if the Au electrode has been previously oxidized (Figure S11A vs Figure S11C−F), which we attribute to different reaction intermediates. Depending on the chosen resting potential, the time required to reduce the surface oxide ranges from several seconds to minutes (Figure 1A, Figures S7 and S8). This observation is in agreement with the literature where the Au oxide reduction reaction has been reported to occur on a broad window of time scales from μs to minutes depending on the applied electrode potential.[6,46,56,57]

EC-SER spectra always represent an ensemble response from multiple SERS-hotspots at the surface.[58] The observed temporal evolution of the spectra is therefore an average signature of the surface reactivity during the AuOx reduction. As the SERS background retains its shape during the electroreduction of the surface, the plasmonic hotspot enhancement can be assumed to remain sufficiently constant throughout the experiments (at constant reduction potential) to allow quantitative analysis of relative peak intensities (Figure S14). The SERS background intensity markedly increases for about 30 s upon reduction onset and then fluctuates about ±10% at longer times. We do not find a correlation between background and band intensities (see the Supporting Information and Figure S14 for background/signal trace comparison) at fixed reduction potentials and thus assume that mere chemical changes are reflected in the spectral signatures.

4.2. Identification of Reaction Intermediates. *4.2.1. OH/OD Intermediates.* The broad and asymmetric peak at ∼594 cm^{-1} seen at 1.6 V vs Pd-H (Figure S15B), which, according to the literature, originates from formed Au oxide species,[19] splits into two peaks after the potential jump to the resting potential: one located at ∼560 cm^{-1} and one at ∼613 cm^{-1}. The 560 cm^{-1} peak can be assigned to Au-OH according to isotope exchange experiments that reveal a difference in the peak position of about 15 cm^{-1}. Assuming adsorbed OH species to behave like a simple harmonic oscillator, we calculate the expected isotopic frequency shift factor to be $\Delta = \sqrt{\frac{m_{OH}}{m_{OD}}} = \sqrt{\frac{16+1}{16+2}} \approx 0.972$. Using this isotopic shift factor, we calculate the expected frequency in D_2O electrolytes for the 560 cm^{-1} peak to be 0.972·560.4 cm^{-1} ≈ 544.7 cm^{-1}, which corresponds very well to the experimentally obtained value of 545.5 ± 2.9 cm^{-1} for Au-OD species. The Weaver group reported a vibrational band at 520−580 cm^{-1} in alkaline media that was attributed to Au-OH.[19,59] In acidic solutions, potential-dependent spectral features around 550−580 cm^{-1} that partly down-shifted upon isotope exchange were observed by the same group, but their origin remained elusive.[59] Our DFT calculations considering the implicit solvent predict that the 560 cm^{-1} peak, assigned to OH species attached to Au adatoms (Figure 2A), is located about 14 cm^{-1} higher than the corresponding Au-OD species. This prediction is perfectly consistent with the experimentally observed difference in the Raman shift and thus confirms the Au-OH/D assignment. While OH-intermediates have been assumed to form during the AuOx reduction in sulfuric acid electrolytes, ours is, to the best of our knowledge, the first spectroscopic observation of adsorbed OH-species in acidic environment to date.

Another intermediate peak is observed experimentally at ∼351 cm^{-1} (Figure 1B) that shows a slight down-shift in the peak position of about 1 to 3 cm^{-1} when comparing H_2O- and D_2O-based electrolyte (Table 1). In alkaline media, a feature at 360−420 cm^{-1} has been attributed to Au-OH stretching.[19,20,59] Our DFT calculations suggest that the 351 cm^{-1} peak originates from Au-OH species in a bridge site surface geometry (Figure S12A,C). The low frequency indicates that these OH species are less strongly bound to the Au surface than the ones with on-top geometry that portray a vibrational shift of 560 cm^{-1}. The calculations predict small frequency differences of 3 to 6 cm^{-1} between adsorbed OH and OD (Figure S12), which we indeed observe experimentally (350.5 cm^{-1} in H_2O vs 347.7 cm^{-1} in D_2O).

The appearance of Au-OH/D species suggests that jumping to 1.2(5) V vs Pd-H, namely, by crossing the potential of zero charge of AuOx of 1.29 V vs Pd-H[45] results in a sufficiently negative shift of the electron chemical potential to trigger proton/deuteron adsorption and OH/D formation. Potential-induced proton adsorption by the oxide surface can be expected to lead to a temporal local depletion of protons in the close vicinity of the surface and increase in surface pH, which in turn temporarily stabilizes the formed Au-OH species. Similar surface pH effects on interfacial reactivity have been observed for (bi)carbonate adsorption in acidic solutions.[60] It was shown that even at low pH (solution pH of 1.1) both carbonate and bicarbonate species can be found on Pt(111) electrodes, while the solution pH changes from 1.5 to 4.4 as well as a function of the applied electrode potential favoring carbonate adsorption at more positive potentials.

https://dx.doi.org/10.1021/acscatal.0c02752
ACS Catal. 2020, 10, 12716−12726

Note, however, that DFT does not predict the Au-OH/D interface structure in Figure 2A to be the thermodynamically most stable one in the applied potential range (Figure S1 and Supporting Information), which explains the challenge to monitor such intermediate species experimentally. In principle, the employed implicit model could underestimate the solvation energy of the adsorbed OH/D species for which hydrogen bonding also plays a role. Nonetheless, if we accounted for an additional stabilization of the interface structures by a downward shift of the corresponding formation-energy curves (Figure S1) by few hundreds of meV, we would still obtain the same qualitative picture, i.e., metastable Au-OH/D.

One possible explanation for the discrepancy between experimental and simulation results is that reaction kinetics are not captured in the interface stability analysis that we have carried out but likely play an important role for the temporal stability of Au-OH/D under the given experimental conditions. Particularly, the temporal increase in surface pH due to potential-induced interfacial proton/deuteron depletion, Au/O place exchange, and (bi)sulfate co-adsorption could play a significant role in the overall reaction kinetics (see the discussion below).

4.2.2. Au Oxide Intermediates. Experimentally, we observe a broad peak at 594 cm^{-1} at 1.6(5) V vs Pd-H during Au oxidation (Figure S15B). The calculations show that surface oxide structures that involve minor Au surface restructuring and that could be classified as oxygen-atom adsorption (Figure S12D−F,I side views) are characterized by maximum frequencies that do not exceed 500 cm^{-1}. Larger frequencies (>550 cm^{-1}) are observed for interfaces where oxygen is found in hollow or subsurface sites, which can be classified as 'entangled' surface-oxide structures. The DFT calculations reveal various frequencies in the region between 580 and 600 cm^{-1} (Table S2), indicating that the broad 594 cm^{-1} peak originates from multiple Au oxide/hydroxide structures, as suggested already by the Weaver group,[19] rather than from single AuOx species. This hypothesis is supported by a recent study of our group based on electrochemical tip-enhanced Raman spectroscopy (EC-TERS) where we have identified at least two distinct Au oxide species, Au_2O_3 and Au_2O, during Au defect oxidation.[61]

After the potential jump to 1.2(5) V vs Pd-H, the broad AuOx peak at ∼594 cm^{-1} splits into two peaks. While the lower 560 cm^{-1} peak is due to Au-OH/D formation, the higher wavenumber peak located at ∼613 cm^{-1} can be attributed to Au oxide according to DFT simulations. The corresponding structure is characterized by Au atoms in a 4-fold coordination with oxygen (Figure 2B) whose computed frequencies (vacuum: 609 cm^{-1}; solvent: 621 cm^{-1}) are very close to the experimentally observed one at 613 cm^{-1}. Such Au in a 4-fold coordination with oxygen is typically found in bulk Au oxide, Au_2O_3.[55] The FWHM of the 613 cm^{-1} peak is substantially narrower (∼28 cm^{-1}) than the one of the initial broad AuOx feature at 594 cm^{-1} (∼130 cm^{-1}). The narrower FWHM of the intermediate points to a structurally more ordered Au oxide compared to the initial one, i.e., the broad mixture of AuOx structures present at 1.6(5) V vs Pd-H seems to converge to a coordination symmetry similar to bulk Au_2O_3 upon reduction. The experimentally observed slightly higher peak position in D_2O electrolyte (617 cm^{-1}) compared to the one in H_2O electrolyte can be explained by partial protonation of the interface structure. Adding H/D atoms to the (unit cell) structure displayed in Figure 2B, the maximum frequencies computed in the implicit solvent are 601 and 602 cm^{-1} for H and D containing surfaces, respectively, (Figure S13). The slight 1 cm^{-1} difference, however, could be within the computational error. We therefore assign the 613 cm^{-1} band tentatively to four-fold O-coordinated AuOx similar to the coordination of bulk Au_2O_3.

The spectral features at ∼752 and ∼ 771 cm^{-1} that appear during AuOx reduction are stable in the peak position (i.e., no overlap within standard deviation, see Table 1) upon electrolyte exchange. While our DFT results do not indicate any vibrational signatures of AuOx in this frequency region, Wang and Andrews calculated a maximum frequency of 770 cm^{-1} for O−Au−O complexes.[50] Au oxide complexes can be expected to form during Au oxide reduction and concomitant Au dissolution[11] but have not been identified to date during electrochemical reduction experiments. Since the frequency stability of the 752 and 771 cm^{-1} peaks suggests that they can be assigned to species that do not contain hydrogen or interact closely with other hydrogen-containing species, contrary to previous assignments from DFT[23] and in accordance with the work by Wang and Andrews, we attribute both peaks to O−Au−O complexes.

4.2.3. (Bi)Sulfate Adsorbates. In addition to the peaks assigned to OH- and oxide-intermediates, Raman bands that can be assigned to (bi)sulfate (SO_4^{2-}; HSO_4^-) ions at the electrode surface appear during the surface reduction after the potential jump (but not on the pristine Au electrode after AuOx reduction). Most of the respective Raman shifts are isotope independent and are thus assigned to SO_4^{2-} modes. The typically very broad FWHM in the range of ∼35 to 90 cm^{-1} indicates a range of energetically nonequivalent adsorption sites at the polycrystalline Au surface. In the following, we refer to the positions of the peak maxima as obtained from Lorentz fits.

The broad mode at 233 cm^{-1} originates from Au−O bonds from adsorbed SO_4^{2-}, analogous to SERS modes observed at 213 and 220 cm^{-1} for Cu- and Ag-(SO_4^{2-}), respectively.[48,49]

For bidendate or higher chelating orders of sulfate adsorption on transition metals, the S−O stretching vibrations can be found between 800 and 1300 cm^{-1}.[49] For example, η^2 (bidendate) coordination geometry of SO_4^{2-} at Pd was found to show a symmetric SO stretch at 865 cm^{-1}.[51] Our DFT calculations predict symmetric S−O(Au) stretches at 836, 839, and 854 cm^{-1} for η^3 (tridendate) coordinated SO_4^{2-} on Au(111) in the implicit solvent (Figure S16; Table S3). As such, we attribute the experimentally observed mode at 853 cm^{-1} to the tridendate ν_1 of adsorbed SO_4^{2-}.

The higher frequency modes at 1031 (cf. mode observed at 1052 cm^{-1} in Cu-based SERS[48]) and 1137 cm^{-1} can be attributed to asymmetric ν_3 normal stretch modes of SO_4^{2-}, according to Mabrouk et al.,[54] likely in a monodendate binding geometry.[49] For tridendate adsorption, even higher asymmetric stretch frequencies up to 1300 cm^{-1} can be expected.[49] Our implicit solvent calculations determine a maximum frequency of 1255 cm^{-1} for the SO group pointing away from the Au surface in the η^3 geometry. Accordingly, we assign the SERS band at 1191 cm^{-1} to an asymmetric SO stretch of tridendately bound SO_4^{2-}. Similar bands were observed previously in electrochemical IR spectroscopy between 1155 and 1220 cm^{-1} [44,45] and in Cu-based SERS at 1200 cm^{-1}.[48]

Interestingly, there is one prominent SERS band at 957 cm^{-1} that can be assigned to sulfate species but shows distinctively different behavior from the other SO_4^{2-} modes in

https://dx.doi.org/10.1021/acscatal.0c02752
ACS Catal. 2020, 10, 12716−12726

that it exhibits a small, but non-negligible difference of 2 cm^{-1} in the Raman shift for H_2O- and D_2O-based electrolytes and a FWHM of 10 cm^{-1}, significantly smaller than the FWHM of the other SO_4^{2-} modes. These observations indicate the involvement of H/D-containing bisulfate species, or strongly H/D-coordinated SO_4^{2-}, in the reduction mechanism in a rather uniform adsorption/interaction configuration at the Au oxide surface. In the literature, there is no agreement to date whether or under which conditions HSO_4^- species could be involved in the Au oxide reduction mechanism in sulfuric acid. Similar modes observed in IR spectra at Au were previously assigned to HSO_4^- species by Shingaya and Ito[52] and Parry et al.[53] or to SO_4^{2-} on Au(111) by Weaver and co-workers.[44] In a recent study, Fang et al. determined sulfate to form an ordered adstructure hydrogen-bonded to water molecules on well-defined Au(111) and assigned the 956 cm^{-1} band to the symmetric stretching mode of SO_4^{2-}--H_2O.[62] Based on the calculation of potential-dependent reaction free energies, the authors further showed that a protonation reaction occurs on the well-defined single crystal moving from above to below 1.12 V vs SHE.

All (bi)sulfate modes are visible simultaneously during the AuOx reduction process. After longer waiting times of 50 to 100 s at 1.2 V vs Pd-H, they disappear into the noise level. This spectral behavior suggests that the (bi)sulfate species are present in a mixed adlayer network with OH and oxide species and play a non-negligible role in the overall reduction mechanism.

4.3. Spectral Oscillations. Interestingly, during the plateau in the $I(t)$ traces, we observe oscillatory behavior in the intensity of both OH and (bi)sulfate species in the time-resolved EC-SER spectra (albeit not in the current traces). Reference time traces recorded at 0.6 V vs Pd-H where a negligible amount of OH or (bi)sulfate species should be present at the surface exhibit no reproducible oscillatory pattern. For both H_2O and D_2O solutions, both SER signals oscillate with a period of 4.2 ± 1.5 s (OH species) and 4.0 ± 2.0 s (sulfate species) out of phase with each other (Figure 3 and Figure S17). The intensity oscillations recorded at the reduction resting potential amount to four and two times the spectral noise level of pristine Au at 0.6 V vs Pd-H up to around 35 s. At later times, the oscillations become more difficult to discern because of the decreasing signal-to-noise of the spectra. Au-OH and (bi)sulfate species appearing and disappearing alternatingly in a regular temporal pattern at the surface during the AuOx reduction process hints toward an oscillatory reaction mechanism.

Interestingly, we find similar $I(t)$ traces compared with the work by Garcia and Koper, who investigated the CO oxidation on Pt single crystals – a rather different system at first glance, although the similarity in shape of the $I(t)$ behavior points toward mechanistic similarities with our study. We speculate that the alternating adsorption of reactive species, such as H^+ and (bi)sulfate, at the reactive AuOx sites compares mechanistically to the blocking of step sites by formed carbonate species and subsequent oxidation of CO at the remaining, less active terrace sites during CO/Pt oxidation.

4.4. AuOx Reduction Mechanism. Based on the detected reaction intermediates as discussed above and literature results, we suggest the following reduction mechanism to take place under the given experimental conditions. For simplicity, we only discuss the H_2O/proton case.

We start from a polycrystalline Au oxide surface with various different oxide structures that is characterized by the broad peak at ~594 cm^{-1}. The potential jump from 1.6 V vs Pd-H, positive of the Au oxidation/AuOx reduction equilibrium potential, E^0, to 1.2 V vs Pd-H (negative of E^0) provides an excess negative charge to the electrode. In a first charge transfer step, protons in the electrochemical double layer (DL) in front of the electrode interact with the O-atoms in the surface layer of the AuOx to form Au-OH species (Figure 4

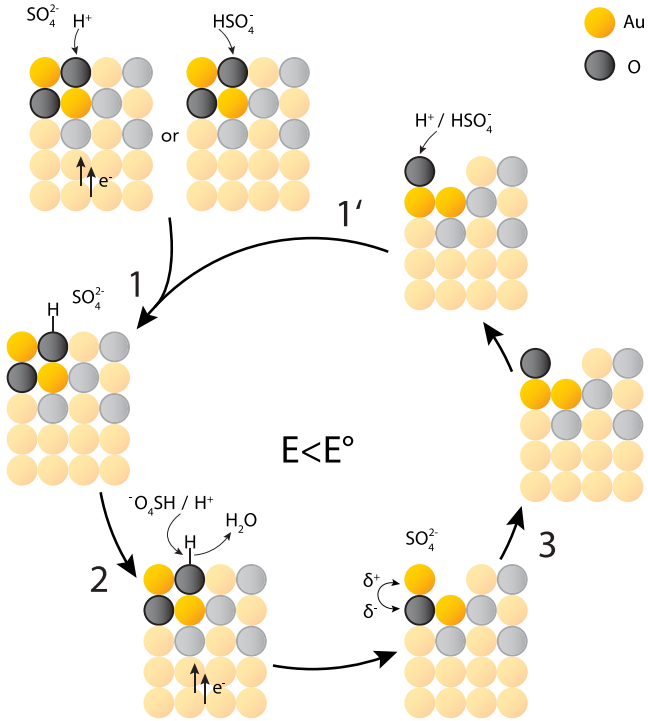

Figure 4. AuOx reduction mechanism. Surface Au oxide is stepwise-reduced via OH-formation as discussed in the main text. Yellow and gray balls represent Au and oxygen atoms, respectively.

step 1). The protons in the DL are available either directly from the acidic solution or can be formed in a dissociation step from near-by bisulfate. The proton depletion in the DL leads to a transient, local increase in pH in close vicinity to the surface that stabilizes the generated Au-OH species sufficiently long to be detectable.[63] At the same time, sulfate anions in the DL start to interact with the partially positively charged Au surface atoms in the AuOx layer.[16]

In a second step, at sufficiently negative resting potentials, OH_{ads} is reduced to water and released into the electrolyte, in agreement with suggestions in the literature (Figure 4 step 2).[12,21,64] Note that we do not observe water bands related to interfacial water species. Water has extremely low Raman scattering cross sections and is thus hard to detect even with SERS. Furthermore, literature findings suggest that interfacial water interacts only weakly with Au surfaces in the explored potential window, which would lead to very low surface enhancement, if any.[65] In the second step, protonation can again occur either directly from hydroxonium ions/protons or from HSO_4^- ions in a concerted proton-abstraction/sulfate adsorption mechanism. The latter is facilitated by the temporal increase of the pH in the DL and a corresponding shift of the $HSO_4^- + OH^- \leftrightarrow SO_4^{2-} + H_2O$ equilibrium toward the right. Neighboring bisulfate and Au-OH surface species can interact,

https://dx.doi.org/10.1021/acscatal.0c02752
ACS Catal. 2020, 10, 12716−12726

leading to a weakly bonded Au-OH species (in line with the observed mode at ~351 cm^{-1}), and form H_2O and SO_4^{2-}. The resulting sulfate participates in the overall AuOx reduction process by temporarily shielding the (partially) positively charged Au following Au−OH bond breaking and H_2O release. Already in 1986, the Conway group anticipated that SO_4^{2-} as a specifically adsorbing anion has a stabilizing effect on AuO(H) species during the electrochemical oxidation of Au single crystals.[21]

The formation of water, i.e., the depletion of O from the surface AuOx layer, results in an Au−O dipole in the subsurface atomic layer. Although this dipole is partly compensated by the charge shielding effects of the SO_4^{2-} ions, its formation triggers an Au-O place exchange[12] and desorption of SO_4^{2-} ions (Figure 4 step 3). As a result, O-atoms from lower layers in the AuOx are in contact with the electrolyte and can be protonated to form Au-OH species, re-initiating the surface reduction process (Figure 4 step 1′). Given the fact that the Au-O place exchange is a fast process, we speculate that the rate-limiting step for the (bi)sulfate/OH turnover is the proton adsorption coupled with the interaction of (bi)sulfate ions with the surface.

The exponential decay term of the employed fit function $I(t)$ of the recorded current traces can be associated with a fast initial AuOx reduction at energetically favorable reduction sites. Only afterward, the interaction between (bi)sulfate anions and formed OH species governs the reduction process, as the locally induced pH variations occur at the interface and an oxide-phase resembling bulk Au_2O_3 is formed. This progressive nucleation-and-growth term is captured by the second term of our employed fit function $I(t)$.

Note that, as investigated by Mayrhofer and co-workers, during the reduction process when surface charge screening by ion adsorption is insufficient, Au species can be dissolved into the electrolyte.[11,66] However, the exact nature of the Au species is unknown and may consist of oxygenated Au species and/or (bi)sulfate-complexed/screened Au, which could explain the observed O−Au−O intermediates.

5. SUMMARY

In summary, we have combined implicit solvent DFT calculations and EC-SERS potential jump experiments to suggest a mechanism for the electro-reduction of AuOx and electrocatalytic formation of surface OH species in sulfuric acid. Importantly, our data confirm the presence of Au-OH intermediates at low pH, a long-standing, but to date unproven hypothesis. Spectral signatures indicate the temporary presence of bisulfate, or a strongly H/D-coordinated sulfate species, in close vicinity to the surface during the oxide reduction, which is debated in the literature. Moreover, we observe regular Au-OH and (bi)sulfate EC-SERS intensity fluctuations with frequencies of around 4 s that indicate an oscillatory reaction mechanism where the formation of Au-OH and its subsequent release as water alternate with the charge shielding by sulfate ions and Au-O place exchange.

From this work, it is obvious that even the presumably simple and often assumed to be well-known electrocatalytic model systems show a level of complexity that demands sophisticated chemical-fingerprint methodology and that it is indeed possible to obtain molecular or even atomistic insights into surface reactions. We propose to extend the EC-SERS potential jump approach to the EC-SHINERS and EC-TERS techniques to gain further insights into well-defined single crystal model electrodes that will ultimately provide further mechanistic understanding of electrocatalytic systems operating at low pH, like metal corrosion, the oxidation of CO, HCOOH, and other small organic molecules, and the OER.

■ ASSOCIATED CONTENT

Supporting Information

The Supporting Information is available free of charge at https://pubs.acs.org/doi/10.1021/acscatal.0c02752.

In-depth stability considerations of DFT computed interface structures, chronoamperometric data recorded during EC-SERS jump experiments, the CV responses of polycrystalline Au in different electrolytes, details on and controls for the potential jump experiments, the fitting of the I/t-traces during AuOx reduction, details on the time-dependent EC-SERS spectral evolution as well as on the data analysis and peak and background fitting procedures, tables with the computed frequencies and Au (hydr)oxide structures, simultaneously recorded CV and EC-SERS data, frequency calculations for adsorbed sulfate, details on the data acquisition and processing of electrochemical measurements, details on the frequency determination of the 560 cm^{-1}-mode oscillations and details on the geometry optimization for the calculations (PDF)

■ AUTHOR INFORMATION

Corresponding Author

Katrin F. Domke − *Molecular Spectroscopy Department, Max Planck Institute for Polymer Research, 55128 Mainz, Germany;* orcid.org/0000-0002-4562-6088; Phone: +49 (0) 6131 379-476; Email: domke@mpip-mainz.mpg.de

Authors

Jonas H. K. Pfisterer − *Molecular Spectroscopy Department, Max Planck Institute for Polymer Research, 55128 Mainz, Germany*

Francesco Nattino − *Theory and Simulations of Materials (THEOS) and National Centre for Computational Design and Discovery of Novel Materials (MARVEL), École Polytechnique Fédérale de Lausanne, 1015 Lausanne, Switzerland*

Ulmas E. Zhumaev − *Molecular Spectroscopy Department, Max Planck Institute for Polymer Research, 55128 Mainz, Germany*

Manuel Breiner − *Molecular Spectroscopy Department, Max Planck Institute for Polymer Research, 55128 Mainz, Germany*

Juan M. Feliu − *Instituto de Electroquímica, Universidad de Alicante, 03080 Alicante, Spain*

Nicola Marzari − *Theory and Simulations of Materials (THEOS) and National Centre for Computational Design and Discovery of Novel Materials (MARVEL), École Polytechnique Fédérale de Lausanne, 1015 Lausanne, Switzerland;* orcid.org/0000-0002-9764-0199

Complete contact information is available at: https://pubs.acs.org/10.1021/acscatal.0c02752

Author Contributions

J.H.K.P., F.N., J.M.F., N.M., and K.F.D. conceived and designed the experiments and simulations. J.H.K.P., U.E.Z., and M.B. carried out the experiments. F.N. performed the simulations. J.H.K.P. and F.N. analyzed the data. J.H.K.P., F.N., N.M., and K.F.D. prepared the manuscript. All authors commented on the manuscript.

Funding

J.H.K.P. and K.F.D. gratefully acknowledge financial support by the Max Planck Graduate Center with the Johannes Gutenberg University Mainz (MPGC). K.F.D. acknowledges generous support through the Emmy Noether Program of the Deutsche Forschungsgemeinschaft (DO1691/1−1) and through the "Plus 3" Program of the Boehringer Ingelheim Foundation. This project has received funding from the European Union's Horizon 2020 research and innovation program under grant agreements No. 665667 and No. 798532. This work was supported by a grant from the Swiss National Supercomputing Centre (CSCS) under project ID s836.

Notes

The authors declare no competing financial interest.

■ ACKNOWLEDGMENTS

We are thankful to Jenée Cyran for valuable scientific discussions and to Stephanie Jung for great graphic design support.

■ REFERENCES

(1) Seh, Z. W.; Kibsgaard, J.; Dickens, C. F.; Chorkendorff, I.; Nørskov, J. K.; Jaramillo, T. F. Combining Theory and Experiment in Electrocatalysis: Insights into Materials Design. *Science* **2017**, *355*, aad4998.

(2) Pombeiro, A. J. L.; Amatore, C. *Trends in Molecular Electrochemistry*; Taylor & Francis Group, 2004, pp 99−376.

(3) Mezzavilla, S.; Cherevko, S.; Baldizzone, C.; Pizzutilo, E.; Polymeros, G.; Mayrhofer, K. J. J. Experimental Methodologies to Understand Degradation of Nanostructured Electrocatalysts for PEM Fuel Cells: Advances and Opportunities. *ChemElectroChem* **2016**, *3*, 1524−1536.

(4) Bandarenka, A. S.; Ventosa, E.; Maljusch, A.; Masa, J.; Schuhmann, W. Techniques and Methodologies in Modern Electrocatalysis: Evaluation of Activity, Selectivity and Stability of Catalytic Materials. *Analyst* **2014**, *139*, 1274.

(5) Meirer, F.; Weckhuysen, B. M. Spatial and Temporal Exploration of Heterogeneous Catalysts with Synchrotron Radiation. *Nat. Rev. Mater.* **2018**, *3*, 324−340.

(6) Bentley, C. L.; Kang, M.; Unwin, P. R. Time-Resolved Detection of Surface Oxide Formation at Individual Gold Nanoparticles: Role in Electrocatalysis and New Approach for Sizing by Electrochemical Impacts. *J. Am. Chem. Soc.* **2016**, *138*, 12755−12758.

(7) Briand, L. E.; Farneth, W. E.; Wachs, I. E. Quantitative Determination of the Number of Active Surface Sites and the Turnover Frequencies for Methanol Oxidation over Metal Oxide Catalysts. *Catal. Today* **2000**, *62*, 219−229.

(8) Taylor, H. S. A. Theory of the Catalytic Surface. *Proc. R. Soc. London A Math Phys. Eng. Sci.* **1925**, *108*, 105−111.

(9) Dong, J.-C.; Zhang, X.-G.; Briega-Martos, V.; Jin, X.; Yang, J.; Chen, S.; Yang, Z.-L.; Wu, D.-Y.; Feliu, J. M.; Williams, C. T.; et al. In Situ Raman Spectroscopic Evidence for Oxygen Reduction Reaction Intermediates at Platinum Single Crystal Surfaces. *Nat. Energy* **2019**, *4*, 60−67.

(10) Zhumaev, U.; Rudnev, A. V.; Li, J. F.; Kuzume, A.; Vu, T. H.; Wandlowski, T. Electro-Oxidation of Au(1 1 1) in Contact with Aqueous Electrolytes: New Insight from in Situ Vibration Spectroscopy. *Electrochim. Acta* **2013**, *112*, 853−863.

(11) Cherevko, S.; Topalov, A. A.; Zeradjanin, A. R.; Katsounaros, I.; Mayrhofer, K. J. J. Gold Dissolution: Towards Understanding of Noble Metal Corrosion. *RSC Adv.* **2013**, *3*, 16516−16527.

(12) Conway, B. E. Electrochemical Oxide Film Formation at Noble Metals as a Surface-Chemical Process. *Prog. Surf. Sci.* **1995**, *49*, 331−452.

(13) Zwaschka, G.; Nahalka, I.; Marchioro, A.; Tong, Y.; Roke, S.; Campen, R. K. Imaging the Heterogeneity of the Oxygen Evolution Reaction on Gold Electrodes Operando: Activity Is Highly Local. *ACS Catal.* **2020**, *10*, 6084−6093.

(14) Man, I. C.; Su, H. Y.; Calle-Vallejo, F.; Hansen, H. A.; Martínez, J. I.; Inoglu, N. G.; Kitchin, J.; Jaramillo, T. F.; Nørskov, J. K.; Rossmeisl, J. Universality in Oxygen Evolution Electrocatalysis on Oxide Surfaces. *ChemCatChem* **2011**, *3*, 1159−1165.

(15) Adić, R. R.; Marković, N. M.; Vešović, V. B. Structural Effects in Electrocatalysis Oxygen Reduction on the Au(100) Single Crystal Electrode. *J. Electroanal. Chem.* **1984**, *165*, 105−120.

(16) Blizanac, B. B.; Arenz, M.; Ross, P. N.; Marković, N. M. Surface Electrochemistry of CO on Reconstructed Gold Single Crystal Surfaces Studied by Infrared Reflection Absorption Spectroscopy and Rotating Disk Electrode. *J. Am. Chem. Soc.* **2004**, *126*, 10130−10141.

(17) Beltramo, G. L.; Shubina, T. E.; Koper, M. T. M. Oxidation of Formic Acid and Carbon Monoxide on Gold Electrodes Studied by Surface-Enhanced Raman Spectroscopy and DFT. *ChemPhysChem* **2005**, *6*, 2597−2606.

(18) Ide, M. S.; Davis, R. J. The Important Role of Hydroxyl on Oxidation Catalysis by Gold Nanoparticles. *Acc. Chem. Res.* **2014**, *47*, 825−833.

(19) Desilvestro, J.; Weaver, M. J. Surface Structural Changes during Oxidation of Gold Electrodes in Aqueous Media as Detected Using Surface-Enhanced Raman Spectroscopy. *J. Electroanal. Chem.* **1986**, *209*, 377−386.

(20) Li, C. Y.; Dong, J. C.; Jin, X.; Chen, S.; Panneerselvam, R.; Rudnev, A. V.; Yang, Z. L.; Li, J. F.; Wandlowski, T.; Tian, Z. Q. In Situ Monitoring of Electrooxidation Processes at Gold Single Crystal Surfaces Using Shell-Isolated Nanoparticle-Enhanced Raman Spectroscopy. *J. Am. Chem. Soc.* **2015**, *137*, 7648−7651.

(21) Angerstein-Kozlowska, H.; Conway, B. E.; Hamelin, A.; Stoicoviciu, L. Elementary Steps of Electrochemical Oxidation of Single-Crystal Planes of Au-I. Chemical Basis of Processes Involving Geometry of Anions and the Electrode Surfaces. *Electrochim. Acta* **1986**, *31*, 1051−1061.

(22) Štrbac, S.; Adžić, R. R.; Hamelin, A. Oxide Formation on Gold Single Crystal Stepped Surfaces. *J. Electroanal. Chem.* **1988**, *249*, 291−310.

(23) Diaz-Morales, O.; Calle-Vallejo, F.; De Munck, C.; Koper, M. T. M. Electrochemical Water Splitting by Gold: Evidence for an Oxide Decomposition Mechanism. *Chem. Sci.* **2013**, *4*, 2334−2343.

(24) Ataka, K.; Osawa, M. In Situ Infrared Study of Water-Sulfate Coadsorption on gold(111) in Sulfuric Acid Solutions. *Langmuir* **1998**, *14*, 951−959.

(25) Ding, S.-Y.; Yi, J.; Li, J.-F.; Ren, B.; Wu, D.-Y.; Panneerselvam, R.; Tian, Z.-Q. Nanostructure-Based Plasmon-Enhanced Raman Spectroscopy for Surface Analysis of Materials. *Nat. Rev. Mater.* **2016**, *1*, 16021.

(26) Shi, C.; Zhang, W.; Birke, R. L.; Lombardi, J. R. Detection of Short-Lived Intermediates in Electrochemical Reactions Using Time-Resolved Surface-Enhanced Raman Spectroscopy. *J. Phys. Chem.* **1990**, *94*, 4766−4769.

(27) Hörmann, N. G.; Andreussi, O.; Marzari, N. Grand Canonical Simulations of Electrochemical Interfaces in Implicit Solvation Models. *J. Chem. Phys.* **2019**, *150*, No. 041730.

(28) Tian, Z. Q.; Ren, B.; Wu, D. Y. Surface-Enhanced Raman Scattering: From Noble to Transition Metals and from Rough Surfaces to Ordered Nanostructures. *J. Phys. Chem. B* **2002**, *106*, 9463−9483.

(29) Giannozzi, P.; Baroni, S.; Bonini, N.; Calandra, M.; Car, R.; Cavazzoni, C.; Ceresoli, D.; Chiarotti, G. L.; Cococcioni, M.; Dabo, I.; Dal Corso, A.; de Gironcoli, S.; Fabris, S.; Fratesi, G.; Gebauer, R.; Gerstmann, U.; Gougoussis, C.; Kokalj, A.; Lazzeri, M.; Martin-Samos, L.; Marzari, N.; Mauri, F.; Mazzarello, R.; Paolini, S.; Pasquarello, A.; Paulatto, L.; Sbraccia, C.; Scandolo, S.; Sclauzero, G.; Seitsonen, A. P.; Smogunov, A.; Umari, P.; Wentzcovitch, R. M. QUANTUM ESPRESSO: A Modular and Open-Source Software Project for Quantum Simulations of Materials. *J. Phys. Condens. Matter* **2009**, *21*, 1−19.

(30) Giannozzi, P.; Andreussi, O.; Brumme, T.; Bunau, O.; Buongiorno Nardelli, M.; Calandra, M.; Car, R.; Cavazzoni, C.; Ceresoli, D.; Cococcioni, M.; Colonna, N.; Carnimeo, I.; Dal Corso, A.; de Gironcoli, S.; Delugas, P.; DiStasio, R. A., Jr.; Ferretti, A.; Floris, A.; Fratesi, G.; Fugallo, G.; Gebauer, R.; Gerstmann, U.; Giustino, F.; Gorni, T.; Jia, J.; Kawamura, M.; Ko, H. Y.; Kokalj, A.; Küçükbenli, E.; Lazzeri, M.; Marsili, M.; Marzari, N.; Mauri, F.; Nguyen, N. L.; Nguyen, H. V.; Otero-de-la-Roza, A.; Paulatto, L.; Poncé, S.; Rocca, D.; Sabatini, R.; Santra, B.; Schlipf, M.; Seitsonen, A. P.; Smogunov, A.; Timrov, I.; Thonhauser, T.; Umari, P.; Vast, N.; Wu, X.; Baroni, S. Advanced Capabilities for Materials Modelling with Quantum ESPRESSO. *J. Phys. Condens. Matter* **2017**, *29*, 465901.
(31) Perdew, J. P.; Burke, K.; Ernzerhof, M. Generalized Gradient Approximation Made Simple. *Phys. Rev. Lett.* **1996**, *77*, 3865−3868.
(32) Dal Corso, A. Pseudopotentials Periodic Table: From H to Pu. *Comput. Mater. Sci.* **2014**, *95*, 337−350.
(33) Kucukbenli, E.; Monni, M.; Adetunji, B. I.; Ge, X.; Adebayo, G. A.; Marzari, N.; de Gironcoli, S.; Corso, A. D.. Projector Augmented-Wave and All-Electron Calculations across the Periodic Table: A Comparison of Structural and Energetic Properties. *arXiv* 2014, No. 1404.3015v1, 1−13.
(34) Schlipf, M.; Gygi, F. Optimization Algorithm for the Generation of ONCV Pseudopotentials. *Comput. Phys. Commun.* **2015**, *196*, 36−44.
(35) Prandini, G.; Marrazzo, A.; Castelli, I. E.; Mounet, N.; Marzari, N.. Precision and Efficiency in Solid-State Pseudopotential Calculations. *arXiv* 2018, No. 1806.05609v2, 1−20, DOI: 10.1038/s41524-018-0127-2.
(36) Andreussi, O.; Marzari, N. Electrostatics of Solvated Systems in Periodic Boundary Conditions. *Phys. Rev. B* **2014**, *90*, 1−16.
(37) Marzari, N.; Vanderbilt, D.; De Vita, A.; Payne, M. C. Thermal Contraction and Disordering of the al(110) Surface. *Phys. Rev. Lett.* **1999**, *82*, 3296−3299.
(38) Andreussi, O.; Nattino, F.; Dabo, I.; Timroy, I.; Fisicaro, G.; Goedecker, S.; Marzari, N. Environ 1.0.
(39) Fattebert, J. L.; Gygi, F. First-Principles Molecular Dynamics Simulations in a Continuum Solvent. *Int. J. Quantum Chem.* **2003**, *93*, 139−147.
(40) Andreussi, O.; Dabo, I.; Marzari, N. Revised Self-Consistent Continuum Solvation in Electronic-Structure Calculations. *J. Chem. Phys.* **2012**, *136*, 064102−064101.
(41) Truscott, M.; Andreussi, O. Field-Aware Interfaces in Continuum Solvation. *J. Chem. Theory Comput.* **2019**, *123*, 3513−3524.
(42) Hjorth Larsen, A.; Jørgen Mortensen, J.; Blomqvist, J.; Castelli, I. E.; Christensen, R.; Dułak, M.; Friis, J.; Groves, M. N.; Hammer, B.; Hargus, C.; Hermes, E. D.; Jennings, P. C.; Bjerre Jensen, P.; Kermode, J.; Kitchin, J. R.; Leonhard Kolsbjerg, E.; Kubal, J.; Kaasbjerg, K.; Lysgaard, S.; Bergmann Maronsson, J.; Maxson, T.; Olsen, T.; Pastewka, L.; Peterson, A.; Rostgaard, C.; Schiøtz, J.; Schütt, O.; Strange, M.; Thygesen, K. S.; Vegge, T.; Vilhelmsen, L.; Walter, M.; Zeng, Z.; Jacobsen, K. W. The Atomic Simulation Environment - A Python Library for Working with Atoms. *J. Phys. Condens. Matter* **2017**, *29*, 27.
(43) Nørskov, J. K.; Rossmeisl, J.; Logadottir, A.; Lindqvist, L.; Kitchin, J. R.; Bligaard, T.; Jónsson, H. Origin of the Overpotential for Oxygen Reduction at a Fuel-Cell Cathode. *J. Phys. Chem. B* **2004**, *108*, 17886−17892.
(44) Edens, G. J.; Gao, X.; Weaver, M. J. The Adsorption of Sulfate on gold(111) in Acidic Aqueous Media: Adlayer Structural Inferences from Infrared Spectroscopy and Scanning Tunneling Microscope. *J. Electroanal. Chem.* **1994**, *375*, 357−366.
(45) Pfisterer, J. H. K.; Zhumaev, U. E.; Cheuquepan, W.; Feliu, J. M.; Domke, K. F. Stark Effect or Coverage Dependence? Disentangling the EC-SEIRAS Vibrational Shift of Sulfate on Au(111). *J. Chem. Phys.* **2019**, *150*, No. 041709.
(46) Vela, M. E.; Salvarezza, R. C.; Arvia, A. J. The Electroreduction Kinetics of the Hydrous Gold Oxide Layers and Growth Modes and Roughness of the Electroreduced Gold Overlayers. *Electrochim. Acta* **1990**, *35*, 117−125.
(47) García, G.; Koper, M. T. M. Mechanism of Electro-Oxidation of Carbon Monoxide on Stepped Platinum Electrodes in Alkaline Media: A Chronoamperometric and Kinetic Modeling Study. *Phys. Chem. Chem. Phys.* **2009**, *11*, 11437−11446.
(48) Brown, G. M.; Hope, G. A. In-Situ Spectroscopic Evidence for the Adsorption of SO_4^{2-} Ions at a Copper Electrode in Sulfuric Acid Solution. *J. Electroanal. Chem.* **1995**, *382*, 179−182.
(49) Outka, D. A.; Madix, R. J.; Fisher, G. B.; DiMaggio, C. Oxidation of Sulfur Dioxide on Ag(110): Vibrational Study of the Structure of Intermediate Complexes Formed. *J. Phys. Chem.* **1986**, *90*, 4051−4057.
(50) Wang, X.; Andrews, L. Precious Metal-Molecular Oxygen Complexes: Neon Matrix Infrared Spectra and Density Functional Calculations for $M(O_2)$, $M(O_2)_2$ (M = Pd, Pt, Ag, Au). *J. Phys. Chem. A* **2001**, *105*, 5812−5822.
(51) Burke, M. L.; Madix, R. J. Formation of Adsorbed Sulfate from the Oxidation of Sulfur Dioxide on Pd(100). *J. Phys. Chem.* **1988**, *92*, 1974−1981.
(52) Shingaya, Y.; Ito, M. Comparison of a Bisulfate Anion Adsorbed on M(111) (M = Pt, Rh, Au, Ag and Cu). *J. Electroanal. Chem.* **1999**, *467*, 299−306.
(53) Parry, D. B.; Samant, M. G.; Seki, H.; Philpott, M. R.; Ashley, K. In Situ Fourier Transform Infrared Spectroelectrochemical Study of Bisulfate and Sulfate Adsorption on Gold, with and without the Underpotential Deposition of Copper. *Langmuir* **1993**, *9*, 1878−1887.
(54) Ben Mabrouk, K.; Kauffmann, T. H.; Aroui, H.; Fontana, M. D. Raman Study of Cation Effect on Sulfate Vibration Modes in Solid State and in Aqueous Solutions. *J. Raman Spectrosc.* **2013**, *44*, 1603−1608.
(55) Jones, P. G.; Rumpel, H.; Sheldrick, G. M.; Schwarzmann, E. Gold(III) Oxide and Oxychloride. *Gold Bull.* **1980**, *13*, 56.
(56) Shrestha, B. R.; Baimpos, T.; Raman, S.; Valtiner, M. Angstrom-Resolved Real-Time Dissection of Electrochemically Active Noble Metal Interfaces. *ACS Nano* **2014**, *8*, 5979−5987.
(57) Giron, R. G. P.; Ferguson, G. S. Development of Cathodic Silence in an Oxide Film on a Gold Electrode. *Electrochim. Acta* **2015**, *180*, 560−563.
(58) Fang, Y.; Seong, N.-H.; Dlott, D. D. Measurement of the Distribution of Site Enhancements in Surface-Enhanced Raman Scattering. *Science* **2008**, *321*, 388−392.
(59) Zhang, Y.; Gao, X.; Weaver, M. J. Nature of Surface Bonding on Voltammetrically Oxidized Noble Metals in Aqueous Media as Probed by Real-Time Surface-Enhanced Raman Spectroscopy. *J. Phys. Chem.* **1993**, *97*, 8656−8663.
(60) Martínez-Hincapié, R.; Berná, A.; Rodes, A.; Climent, V.; Feliu, J. M. Surface Acid-Base Properties of Anion-Adsorbed Species at Pt(111) Electrode Surfaces in Contact with CO2-Containing Perchloric Acid Solutions. *J. Phys. Chem. C* **2016**, *120*, 16191−16199.
(61) Pfisterer, J. H. K.; Baghernejad, M.; Giuzio, G.; Domke, K. F. Reactivity Mapping of Nanoscale Defect Chemistry under Electrochemical Reaction Conditions. *Nat. Commun.* **2019**, *10*, 1−8.
(62) Fang, Y.; Ding, S.-Y.; Zhang, M.; Steinmann, S. N.; Hu, R.; Mao, B.-W.; Feliu, J. M.; Tian, Z.-Q. Revisiting the Atomistic Structures at the Interface of Au(111) Electrode−Sulfuric Acid Solution. *J. Am. Chem. Soc.* **2020**, *142*, 9439−9446.
(63) Ogura, K.; Haruyama, S.; Nagasaki, K. The Electrochemical Oxidation and Reduction of Gold. *J. Electrochem. Soc.* **1971**, *118*, 531−535.
(64) Peuckert, M.; Coenen, F. P.; Bonzel, H. P. On the Surface Oxidation of a Gold Electrode in 1N H_2SO_4 Electrolyte. *Surf. Sci.* **1984**, *141*, 515−532.
(65) Tong, Y.; Lapointe, F.; Thämer, M.; Wolf, M.; Campen, R. K. Hydrophobic Water Probed Experimentally at the Gold Electrode/Aqueous Interface. *Angew. Chem. Int. Ed.* **2017**, *56*, 4211−4214.
(66) Cherevko, S.; Zeradjanin, A. R.; Keeley, G. P.; Mayrhofer, K. J. J. A Comparative Study on Gold and Platinum Dissolution in Acidic and Alkaline Media. *J. Electrochem. Soc.* **2014**, *161*, H822−H830.